Tailoring Third Harmonic Generation From Anapole Mode in a Metal-Dielectric Hybrid Nanoantenna

Yan Yin, Jin Yao [ID], Longfang Ye [ID], Guoxiong Cai [ID], *Member, IEEE*, and Qing Huo Liu [ID], *Fellow, IEEE*

Abstract—An all-dielectric nanoantenna is expected to greatly boost the nonlinear performance owing to its large mode volume and low material loss. However, it still suffers from the relatively weak near-field enhancement and the inferior far-field directivity. In this work, by successively introducing an upper metal ring and a bottom metal film, the plasmonic resonance and the perfect electric conductor (PEC) mirror effect are employed to significantly enhance and tailor the third harmonic generation (THG) from the high-index silicon nanoantenna. Numerical results show that benefiting from both of these two metal components, not only the THG efficiency is increased by more than 1 and 3.5 orders of magnitude compared with those with only single metal component and without any metal component, respectively, but also an improved radiation directivity can be obtained. The dependences of geometric parameters are discussed as well. This work suggests a route to enhance and manipulate the nonlinear radiation by a hybrid nanoantenna and facilitates its practical applications such as biosensing and nonlinear light sources.

Index Terms—Optical nanoantenna, third harmonic generation, nonlinear far-field scattering.

I. INTRODUCTION

THE combination of nanotechnology and near-field optics has led to the emergence of a new discipline, nanophotonics, in the high-tech field. As one of its branches, nonlinear nanophotonics aims to manipulate the interaction between light and matter in a nonlinear manner at the nanoscale [1]. By exchanging energy between photons, various nonlinear responses, such as harmonic generation [2]–[5], spontaneous emission [6] and optical bistability [7], [8], etc., have been widely employed in frequency conversion [9], quantum sources [10] and biosensing [11].

Yan Yin, Jin Yao, Longfang Ye, and Guoxiong Cai are with the Institute of Electromagnetics and Acoustics, Fujian Provincial Key Laboratory of Electromagnetic Wave Science and Detection Technology, Xiamen University, Xiamen 361005, China (e-mail: 2321238989@qq.coh; yj12666@163.com; lfye@xmu.edu.cn; gxcai8303@xmu.edu.cn).

Qing Huo Liu is with the Department of Electrical and Computer Engineering, Duke University, Durham, NC 27708 USA (e-mail: qhliu@duke.edu).

Third harmonic generation (THG) is a process coherently tripling the energy of an incident photon. Since THG possesses the cube relation with the field intensity, its performance could be intensively boosted by enhancing the local field [1], [12]. Nanoantennas and nanoparticles made from high-refractive-index dielectrics have been reported to enlarge the mode volume, reduce the loss, and thus boost the nonlinear performance of the optical systems [13]–[15]. These high-refractive-index dielectrics allow not only low losses but also strong near field enhancements due to the presence of electric and magnetic multipole modes [16], [17]. Recently, anapole mode originating from the destructive interference of Cartesian electric dipole [ED(C)] and toroidal dipole (TD) moments [18], [19] has been employed to intensively enhance the near field and improve the THG efficiency. THG conversion efficiency of 0.0001% has been achieved by the anapole mode in the all-dielectric germanium nanosystem [20]. By involving different kinds of metal components, the anapole modes can be enhanced and their THG efficiencies can be improved to be 0.007% and 0.01%, respectively [21], [22]. However, THG efficiency is still limited by the relatively mild enhancement of anapole mode, requiring further designs of the nonlinear nanoantennas.

Optical nanoantenna is one of the hot research fields of micro-nano optics, which has been widely applied in lasers [23], [24], photodetection [25], biological imaging and sensing [26], [27]. As a key factor in optical nanoantennas, directionality determines the efficiency of collecting the radiative energy. Many researches have been reported to improve the directionality of nonlinear far-field scattering from nanoantennas. By manipulating the pump beam polarization, incident angle and geometric parameters, the nonlinear far-field scattering can be effectively tailored [28]. The directivity of the nonlinear scattering can also be improved based on the integration of holographic gratings [29]. However, the current nanoantenna still faces the problem of further improving the directivity. On the other hand, the existing research on nonlinear far-field radiation mainly focuses on the second harmonic generation (SHG), and the radiation pattern of THG is barely investigated and requires more exploration.

In this work, we propose a metal-dielectric hybrid nanoantenna with a THG efficiency 5.7×10^{-4} under pump intensity $I_0 = 0.5 \, \text{GW/cm}^2$ and a tailored nonlinear far-field scattering. First, by successively involving two metal components, the process of
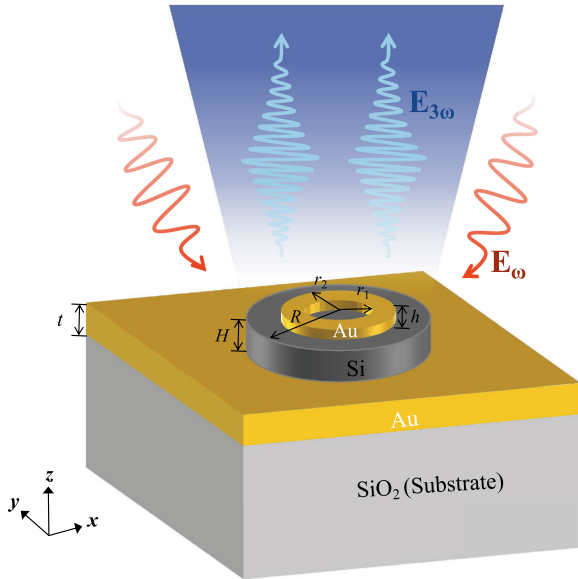
Fig. 1. Schematic diagram of the proposed metal-dielectric hybrid nanoantenna. The silicon nanodisk is sandwiched by an Au ring and an Au film. THG originates from the silicon with third-order susceptibility. Geometric parameters: radius $R = 460$ nm and height $H = 190$ nm of silicon nanodisk, inner radius r_1, outer radius r_2, and height $h = 50$ nm of Au nanoring, and thickness $t = 200$ nm of Au film. Yellow material corresponds to Au, while dark gray material corresponds to silicon.
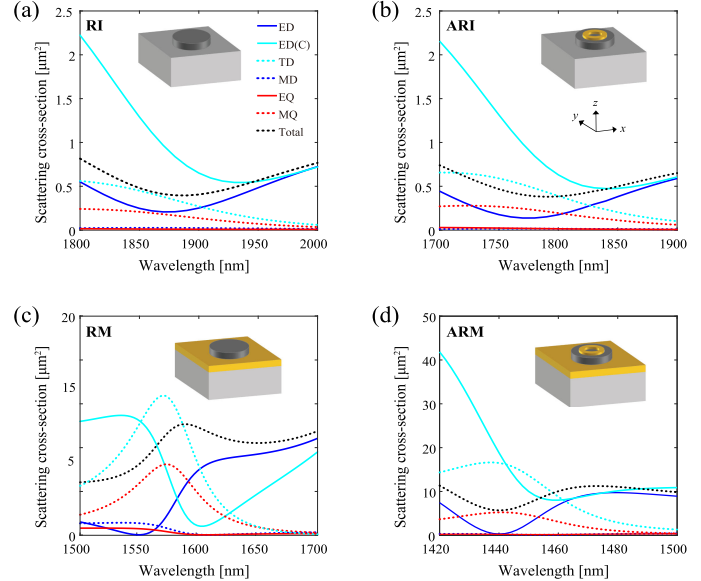

Fig. 2. Multipolar decompositions of scattering cross-section (SCS) spectra. (a)–(d) are a resonator on insulator (RI), Au ring on a resonator on insulator (ARI), a resonator on metal (RM) and Au ring on a resonator on metal (ARM), respectively. ED, ED(C), TD, MD, EQ, MQ and Total denote electric dipole, Cartesian electric dipole, toroidal dipole, magnetic dipole, electric quadrupole, magnetic quadrupole and total SCS. Insets are schematic diagrams of their corresponding structure. Au nanoring has an inner radius $r_1 = 65$ nm and outer radius $r_2 = 300$ nm. Other parameters are the same as those in Fig. 1.

enhancing the anapole mode is demonstrated. Then, benefited by the double metal components, the THG from the proposed metal-dielectric hybrid nanoantenna is increased by 3.5 orders of magnitude compared with that without any metal component. Finally, by optimizing the geometric parameters, the nonlinear radiation patterns are tailored, achieving a preeminent directivity performance.

II. STRUCTURE DESIGN AND PHYSICAL MECHANISM

Fig. 1 depicts the schematic of the proposed metal-dielectric hybrid nanoantenna, which consists of a silicon nanodisk sandwiched by an Au nanoring and an Au uniform film. It is placed on an infinite SiO_2 substrate with the refractive index $n = 1.47$. The dispersive refractive indexes of Au and silicon are extracted from their corresponding experimental data [30], [31], respectively. Hydrogenated amorphous silicon is selected here because of its high refractive index and high nonlinear coefficient in the near-infrared band, as well as excellent large-scale preparation compatibility [32]. Linear and nonlinear responses are both numerically simulated by commercial software COMSOL Multiphysics^{TM} based on the finite element method. For both linear and nonlinear simulations, perfectly matched layers around the nanoparticle are employed to simulate the infinite open space. We assumed the undepleted pump field approximation and followed two steps to model the nonlinear response [33], [34]. On the other hand, the Cartesian multipole expansion [35] is performed using the polarization in silicon which is numerically obtained. The practical fabrication can be readily accomplished by the combination of evaporation, silicon

deposition, electron-beam lithography and reactive-ion etching techniques [21], [36].

In order to study the effects of metal, the structure of a single all-dielectric silicon nanodisk is considered first and then two metal components are successively introduced. With normal illumination of the x-polarized plane wave, Figs. 2(a)–(d) give the multipolar decompositions of scattering cross-sections (SCSs) for four different structures, i.e., a resonator on insulator (RI), Au ring on a resonator on insulator (ARI), a resonator on metal (RM) and Au ring on a resonator on metal (ARM), respectively. Their schematic diagrams are shown in the corresponding insets, respectively. For fair comparison, the size of silicon nanodisks in four structures is the same. This size of silicon nanodisks is chosen to obtain a clear anapole mode for the ARM structure, and to simultaneously achieve anapole modes for all these four structures. Therefore, the anapole modes in Figs. 2(a) and (b) have EDs with non-zero dips. In Fig. 2(a), an ED dip can be observed at wavelength $\lambda = 1860$ nm, which originates from the destructive interference between ED(C) and TD moments, indicating the excitation of an anapole mode [22]. Then, by respectively introducing an upper metal ring and a lower metal film [shown by the insets in Figs. 2(b) and (c)], the plasmonic resonance and the perfect electric conductor (PEC) mirror effect are involved to facilitate the anapole modes [21], [22]. Two ED dips in Figs. 2(b) and (c) respectively indicate that the scattering nature of an anapole mode can still be found at the similar wavelength range yet with slight blue-shifts when comparing to Fig. 2(a), and the Au film leads to blue shifting more. Finally, the upper Au ring and the lower Au film are added simultaneously. It can be seen in Fig. 2(d) that although the ED dip is influenced
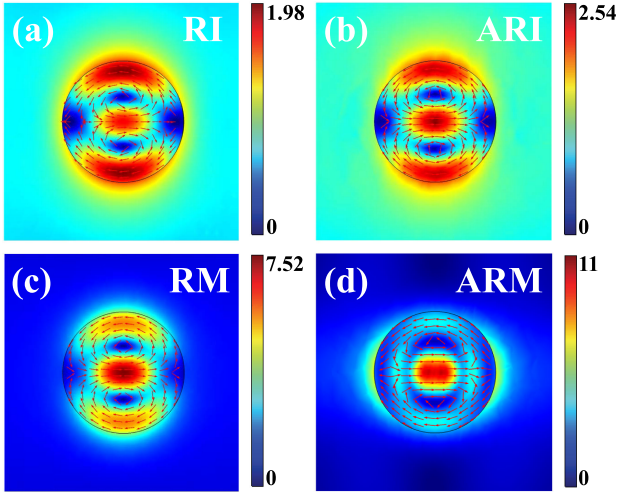
Fig. 3. Electric field distributions $|E/E_{\text{inc}}|$ in *xy*-plane normalized to the incidence. The cut planes are located at the middle of the silicon nanodisks. Red arrows represent the current directions. (a)–(d) are RI, ARI, RM, and ARM, respectively. Results are extracted from their corresponding resonant wavelengths of anapole modes.

by the permittivity of both Au components and thus blue shifts to 1440 nm, the scattering nature of an anapole mode is still not changed.

To investigate the contributions of metal components to the near field, Figs. 3(a)–(d) give the normalized electric field distributions and the current directions inside silicon nanodisks for these four cases. For the RI structure in Fig. 3(a), with two current loops circulating in opposite direction, three electric hotspots can be found inside the silicon nanodisk. Fig. 3(a) demonstrates the typical electromagnetic distributions of an anapole mode. When the Au ring is introduced separately to form the ARI structure in Fig. 3(b), the nature of electromagnetic distributions of the anapole mode is reserved, and the plasmonic resonance excited by the Au ring [21] increases the electric field enhancement inside the silicon disk. When the Au film is introduced separately to form the RM structure in Fig. 3(c), since the metal film acts as a mirror with PEC mirror effect [22], [37], the electric field of anapole mode is strongly enhanced and is more concentrated inside the silicon nanodisk. Finally, combining both advantages of these two metal components, the electric field of ARM in Fig. 3(d) is much more localized toward the center of the nanodisk yet still retains the characteristics of anapole mode. Benefiting from both the plasmonic resonance and the PEC mirror effect by these two metal components, the electric field inside silicon is greatly enhanced with a maximum enhancement factor $|E_{\text{max}}/E_{\text{inc}}| = 11$, more than 5 times as large as that of RI structure in Fig. 3(a), which promises a preeminent nonlinear performance.

III. ENHANCED THG EFFICIENCY BY DOUBLE METAL COMPONENTS

In order to fully explore the effect of the double metal components on the THG efficiency, the influence of inner radius r_1 and outer radius r_2 of the Au ring in the ARM structure is

presented in Fig. 4(a). For nonlinear simulation, THG is calculated based on an undepleted pump approximation. We used two steps to obtain the nonlinear emission. By simulating the linear scattering at the fundamental wavelength, the nonlinear polarization induced inside the nanodisk is obtained. Then, the obtained nonlinear polarization is employed as a source term at the harmonic wavelength to simulate the generated TH field. All the THG efficiencies are taken from the corresponding anapole resonant wavelengths. Silicon is a nonlinear material with the almost constant third-order susceptibility $\chi^{(3)} = 2.45 \times 10^{-19}$ $(\text{m/V})^2$ around wavelength 1550 nm [22]. The induced nonlinear polarization components at the third harmonic (TH) wavelength can be calculated as $\mathbf{P}^{(3)} = \varepsilon_0 \chi^{(3)} (\mathbf{E} \cdot \mathbf{E}) \mathbf{E}$, where ε_0 is the vacuum permittivity, and $\mathbf{E}$ is the electric field inside silicon at the fundamental wavelength. After solving electromagnetic field at the TH wavelength via $\mathbf{P}^{(3)}$, the THG efficiency of a nanoantenna is then defined as [37]

$$\eta_{\text{THG}} = \frac{\int_A \vec{S}_{\text{TH}} \cdot \hat{n} \, \mathrm{d}a}{I_0 \times \pi r^2} \tag{1}$$

where I_0 is the pump intensity, $\vec{S}$ is the Poynting vector of the TH field, and $\hat{n}$ is the unit vector normal to a surface A enclosing the silicon nanoparticle. With pump intensity $I_0 = 0.5 \text{ GW/cm}^2$, Fig. 4(a) shows that the THG efficiency 5.7×10^{-4} of ARM structure is optimized at $r_1 = 65$ nm, $r_2 = 330$ nm. It should be noted that the anapole mode at the fundamental frequency remains unchanged despite the change of the Au ring. The obtained THG efficiency is among the highest achieved to date under the similar pump intensity. For the single silicon nanoparticle, the current highest THG efficiency is 10^{-4} under pump intensity 1 GW/cm^2 [20], while for silicon periodic array, it is 10^{-2} under pump intensity 2 GW/cm^2 [36]. As the pump intensity further increases, these THG efficiencies could be theoretically raised with a square relation. However, in practical operations, they possess a saturation value due to the influence of photo-induced nonlinear effects, such as Kerr effect [8]. Furthermore, THG efficiency would be subject to the peak intensity, pulse duration and repetition rate of the pump laser beam [38].

The histogram in Fig. 4(b) describes the THG efficiencies corresponding to these four structures, where ARI and ARM are the results obtained under the optimal size of the ring. It can be seen that as compared with the RI structure, the THG efficiency of the ARI structure is improved by almost one order of magnitude while that of the RM structure is enhanced by more than two orders of magnitude, implying the more contribution of PEC mirror effect from metal film to the THG efficiency. Moreover, dedicated by the doubly enhanced anapole mode, the THG efficiency of the ARM structure is more than 3.5 orders of magnitude compared with that of the RI structure, and it is at least one order of magnitude higher than that of the RM structure. The latter in our work is comparable to the similar structure which has the reported highest THG efficiencies [22]. In order to reveal the factor affecting the THG capability, we further evaluate the four structures' abilities to concentrate the electric field inside the silicon disk, which is quantified by the average electric field
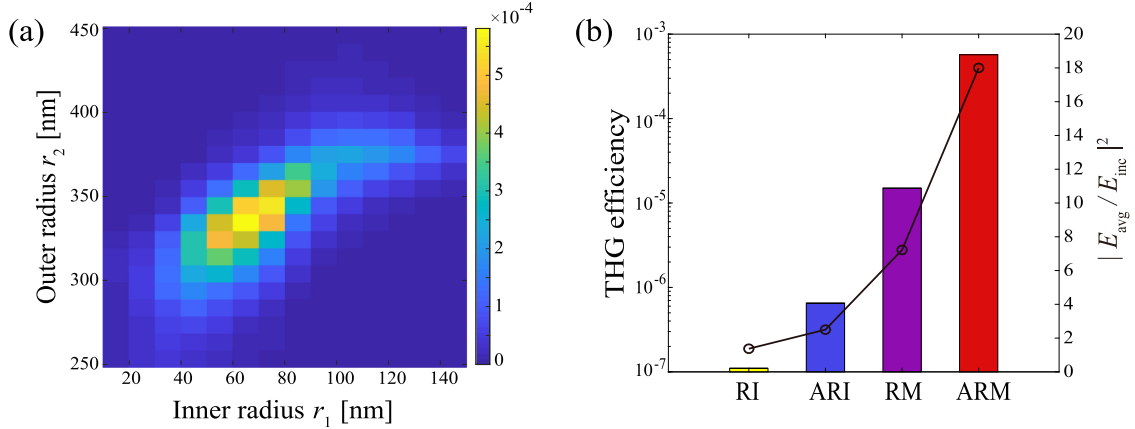
Fig. 4. (a) Dependence of THG efficiency on inner radius r_1 and outer radius r_2 of the Au ring in the ARM structure. (b) THG efficiencies of four cases, RI, ARI, RM, and ARM. Geometric parameters of these four cases are $r_1 = 60$ nm, $r_2 = 100$ nm in the ARI structure. $r_1 = 65$ nm, $r_2 = 330$ nm in the ARM structure, which have been optimized to achieve their corresponding highest efficiencies. The black polyline describes the average electric field enhancement factors inside the silicon nanodisk.
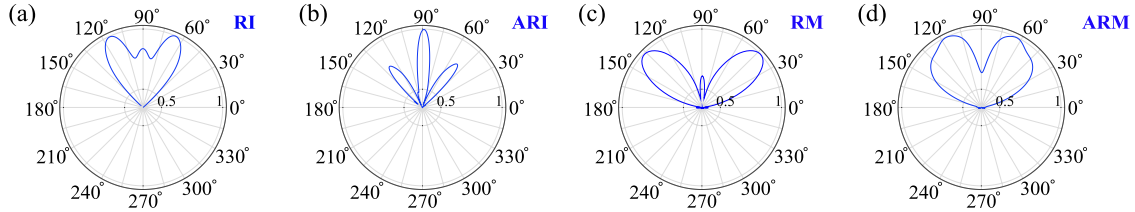

Fig. 5. Nonlinear THG far-field radiation patterns in the yz plane. (a)–(d) are RI, ARI, RM, and ARM, respectively. The geometric parameters of these four structures are the same as those in Fig. 4(b).

enhancement factor as following [8]

$$|E_{\mathrm{avg}}/E_{\mathrm{inc}}|^2 = \frac{\iiint |E|^2 \mathrm{d}V}{|E_{\mathrm{inc}}|^2 V} \qquad (2)$$

where E and V denote the local electric field inside the silicon disk and the volume of it, respectively, and E_{inc} is the amplitude of incident electric field. The black polyline in Fig. 4(b) describes the average enhancement factor inside the silicon nanodisk for these four structures, and the values of the average enhancement factor are positively correlated with nonlinear performance. One of the key factors to boost THG from nanoscale is to increase the average enhancement factor inside the nonlinear materials.

IV. TAILORED RADIATION PATTERN BY GEOMETRIC PARAMETERS

In practical operations, the directivity of radiation determines whether the energy can be effectively collected due to the limited numerical aperture values. To investigate the directivities of THG radiation in these four cases, Fig. 5 gives their nonlinear far-field radiation patterns with only backscattering direction considered for a convenient comparison, which is numerically calculated by COMSOL and the far-field domain is located at the surface of a cube with side length of 1800 nm. Since the radiation patterns are mainly contributed in the yz plane, we mainly compare the directional patterns of the yz plane and

those of xz plane are not presented for simplicity. For the RI structure in Fig. 5(a), there are three lobes in the backscattering direction, but the radiation of two side lobes is larger than that of the middle lobe. By involving the upper metal ring, the middle lobe can be greatly enhanced, as shown in Fig. 5(b), indicating a high directivity for the ARI case. For RM structure in Fig. 5(c), although the metal film can strongly boost the THG efficiency as discussed above, it has little contribution to the directivity. Its middle lobe is suppressed, and the angle between two side lobes is even larger. For ARM structure, benefiting from the upper metal ring, the angle between two side lobes is reduced, but the middle lobe is still suppressed, which requires further adjustment on its geometric parameters.

The nonlinear far-field radiation patterns corresponding to the different inner and outer radii of the Au ring are thus investigated in Fig. 6. It can be seen in Fig. 6(a) that the increase of the inner radius can gradually concentrate the radiation to the normal backward direction. When $r_1 = 150$ nm, the middle lobe dramatically inflates with the side lobes being suppressed, indicating a great directivity for this geometric parameter. As r_1 continues to increase, the directivity deteriorates. For the outer radius, as can be seen in Fig. 6(b), higher directivity can be obtained with larger r_2, but it has little effect on the directivity of the far-field radiation. Finally, after going through the parameter space, the optimized directivity is found at $r_1 = 170$ nm, $r_2 = 370$ nm.
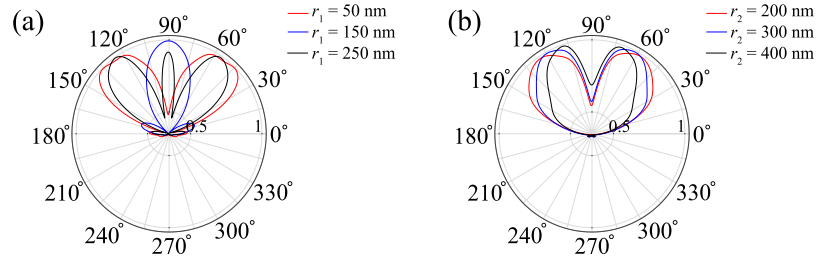
Fig. 6. Dependences of nonlinear THG far-field radiation patterns in the yz plane on (a) inner radius r_1 and (b) outer radius r_2 of the Au ring in the ARM structure. $r_2 = 330$ nm is fixed in Fig. 6(a), while $r_1 = 65$ nm is fixed in Fig. 6(b).
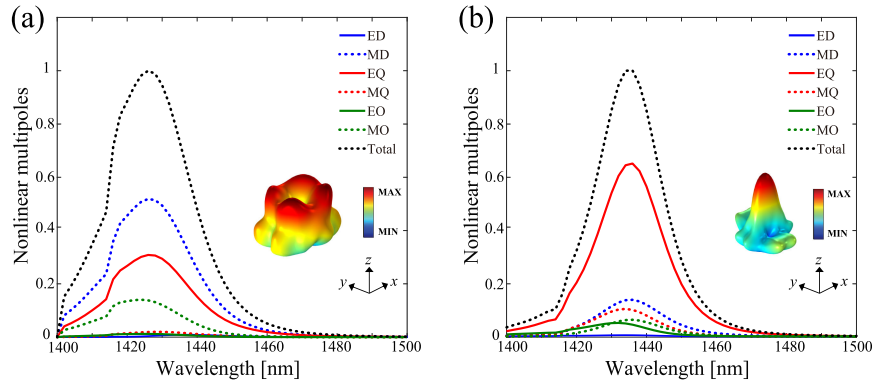

Fig. 7. Nonlinear multipolar decompositions of THG scattering for two ARM structures with (a) the largest efficiency and (b) the optimal directivity, respectively. $r_1 = 65$ nm, $r_2 = 330$ nm in Fig. 7(a), while $r_1 = 170$ nm, $r_2 = 370$ nm in Fig. 7(b). EO and MO denote electric octupole and magnetic octupole. Insets are 3D images of their corresponding nonlinear far-field radiations.

To further investigate the mechanism, the nonlinear multipolar decompositions and the nonlinear far-field radiation patterns for two ARM structures, where one has the largest efficiency and the other has the optimal directivity, are given in Figs. 7(a) and (b), respectively. The nonlinear multipoles in Fig. 7 are calculated based on the multipolar decompositions of the nonlinear light-induced polarization inside silicon at TH wavelength [39]. In Fig. 7(a), although the efficiency is the largest, three moments, i.e., magnetic dipole (MD), electric quadrupole (EQ) and magnetic octupole (MO) play important roles in its nonlinear scattering, resulting in a radiation pattern that has many side lobes. In Fig. 7(b), its nonlinear scattering is dominated by the EQ moment, and radiations on the sides are suppressed, showing an outstanding capability of the unidirectional THG scattering as shown in the inset of Fig. 7(b). However, the THG efficiency under optimal directivity is 1.3×10^{-4}. It shows that the metal ring can be used to optimize either efficiency or directivity, but it is difficult to optimize both properties at the same time. Nevertheless, the THG efficiency at the optimal directivity is still almost one order of magnitude higher than that of the RM structure, and the efficiency of the latter in our work is similar to the highest reported efficiency [22].

V. CONCLUSION

In summary, we have demonstrated that by introducing two metal components, i.e., an upper Au ring and a bottom Au

film, both plasmonic resonance and PEC mirror effect can be introduced, resulting in the improved nonlinear performance of the silicon nanoantenna. Numerical results show that the THG efficiency of ARM structure is 5.7×10^{-4} under pump intensity $I_0 = 0.5$ GW/cm^2, which is among the highest THG efficiencies achieved to date under the similar pump intensity. Furthermore, by changing the parameters of the inner radius and outer radius of the Au ring, the directivity of its far-field radiation can be optimized to nearly normal backscattering. This work broadens the way to efficiently enhance and tailor the THG from nanoantenna, and provides promising prospects for its applications in biological sensing, light sources and many other aspects.

REFERENCES

[1] D. Smirnova and Y. S. Kivshar, "Multipolar nonlinear nanophotonics," *Optica*, vol. 3, no. 11, pp. 1241–1255, 2016.

[2] L. Carletti, A. Locatelli, O. Stepanenko, G. Leo, and C. De Angelis, "Enhanced second-harmonic generation from magnetic resonance in AlGaAs nanoantennas," *Opt. Exp.*, vol. 23, no. 20, pp. 26544–26550, 2015.

[3] Y. Liu, S. Zhu, Q. Zhou, Y. Cao, and Y. Xu, "Giant third-harmonic generation induced by nonlinear field resonances in plasmonic-graphene metasurfaces," *Opt. Exp.*, vol. 28, no. 9, pp. 13234–13242, 2020.

[4] K. Chen, C. Durak, J. R. Heflin, and H. D. Robinson, "Plasmon enhanced second-harmonic generation from ionic self-assembled multilayer films," *Nano Lett.*, vol. 7, no. 2, pp. 254–258, 2007.

[5] R. Franchi, C. Castellan, M. Ghulinyan, and L. Pavesi, "Second-harmonic generation in periodically poled silicon waveguides with lateral p-i-n junctions," *Opt. Lett.*, vol. 45, no. 12, pp. 3188–3191, 2020.

[6] T. Brandes and B. Kramer, "Spontaneous emission of phonons by coupled quantum dots," *Phys. Rev. Lett.*, vol. 83, no. 15, pp. 3021–3024, 1999.

[7] P. Y. Chen, M. Farhat, and A. Alu, "Bistable and self-tunable negative-index metamaterial at optical frequencies," *Phys. Rev. Lett.*, vol. 106, no. 10, 2011, Art. no. 105503.

[8] J. Yao, Y. Wu, J. Liu, N. Liu, and Q. H. Liu, "Enhanced optical bistability by coupling effects in magnetic metamaterials," *J. Lightw. Technol.*, vol. 37, no. 23, pp. 5814–5820, 2019.

[9] H. Jiang, H. Liang, L. Rui, X. Chen, Y. Chen, and L. Qiang, "Nonlinear frequency conversion in one dimensional lithium niobate photonic crystal nanocavities," *Appl. Phys. Lett.*, vol. 113, no. 2, 2018, Art. no. 021104.

[10] C. Navarrete-Benlloch, E. Roldán, Y. Chang, and T. Shi, "Regularized linearization for quantum nonlinear optical cavities: Application to degenerate optical parametric oscillators," *Opt. Exp.*, vol. 22, no. 20, pp. 24010–24023, 2014.

[11] J. R. Ott, M. Heuck, C. Agger, P. D. Rasmussen, and O. Bang, "Label-free and selective nonlinear fiber-optical biosensing," *Opt. Exp.*, vol. 16, no. 25, pp. 20834–20847, 2009.

[12] M. Lippitz, M. A. Van Dijk, and M. Orrit, "Third-harmonic generation from single gold nanoparticles," *Nano Lett.*, vol. 5, no. 4, pp. 799–802, 2005.

[13] V. F. Gili *et al.*, "Monolithic AlGaAs second-harmonic nanoantennas," *Opt. Exp.*, vol. 24, no. 14, pp. 15965–15971, 2016.

[14] E. V. Melik-Gaykazyan *et al.*, "Selective third-harmonic generation by structured light in Mie-resonant nanoparticles," *ACS Photon.*, vol. 5, no. 3, pp. 728–733, 2018.

[15] M. R. Shcherbakov *et al.*, "Enhanced third-harmonic generation in silicon nanoparticles driven by magnetic response," *Nano Lett.*, vol. 14, no. 11, pp. 6488–6492, 2014.

[16] M. Caldarola *et al.*, "Non-plasmonic nanoantennas for surface enhanced spectroscopies with ultra-low heat conversion," *Nature Commun.*, vol. 6, no. 1, 2015, Art. no. 7915.

[17] A. I. Barreda, J. M. Saiz, F. González, F. Moreno, and P. Albella, "Recent advances in high refractive index dielectric nanoantennas: Basics and applications," *AIP Adv.*, vol. 9, no. 4, 2019, Art. no. 040701.

[18] A. Ahmadivand, M. Semmlinger, L. Dong, B. Gerislioglu, P. Nordlander, and N. J. Halas, "Toroidal dipole-enhanced third harmonic generation of deep ultraviolet light using plasmonic meta-atoms," *Nano Lett.*, vol. 19, no. 1, pp. 605–611, 2019.

[19] A. Ahmadivand, B. Gerislioglu, R. Ahuja, and Y. K. Mishra, "Toroidal metaphotonics and metadevices," *Laser Photon. Rev.*, vol. 14, no. 11, 2020, Art. no. 1900326.

[20] G. Grinblat, Y. Li, M. P. Nielsen, R. F. Oulton, and S. A. Maier, "Enhanced third harmonic generation in single germanium nanodisks excited at the anapole mode," *Nano Lett*, vol. 16, no. 7, pp. 4635–4640, 2016.

[21] T. Shibanuma, G. Grinblat, P. Albella, and S. A. Maier, "Efficient third harmonic generation from metal-dielectric hybrid nanoantennas," *Nano Lett.*, vol. 17, no. 4, pp. 2647–2651, 2017.

[22] L. Xu *et al.*, "Boosting third-harmonic generation by a mirror-enhanced anapole resonator," *Light Sci. Appl.*, vol. 7, no. 1, 2018, Art. no. 44.

[23] H. T. Hattori, Z. Li, D. Liu, I. D. Rukhlenko, and M. Premaratne, "Coupling of light from microdisk lasers into plasmonic nano-antennas," *Opt. Exp.*, vol. 17, no. 23, pp. 20878–20884, 2009.

[24] Z. Li, H. T. Hattori, F. Lan, H. H. Tan, and C. Jagadish, "Merging photonic wire lasers and nanoantennas," *J. Lightw. Technol.*, vol. 29, no. 18, pp. 2690–2697, Sep. 2011.

[25] H. T. Miyazaki, T. Mano, T. Kasaya, H. Osato, and H. Miyazaki, "Synchronously wired infrared antennas for resonant single-quantum-well photodetection up to room temperature," *Nature Commun.*, vol. 11, no. 1, 2020, Art. no. 565.

[26] A. Singh, J. T. Hugall, G. Calbris, and N. F. Van Hulst, "Fiber-based optical nanoantennas for single-molecule imaging and sensing," *J. Lightw. Technol.*, vol. 33, no. 12, pp. 2371–2377, Jun. 2015.

[27] R. Arppe *et al.*, "Photon upconversion sensitized nanoprobes for sensing and imaging of pH," *Nanoscale*, vol. 6, no. 12, pp. 6837–6843, 2014.

[28] L. Carletti, A. Locatelli, D. Neshev, and C. De Angelis, "Shaping the radiation pattern of second-harmonic generation from AlGaAs dielectric nanoantennas," *ACS Photon.*, vol. 3, no. 8, pp. 1500–1507, 2016.

[29] L. Ghirardini *et al.*, "Shaping the nonlinear emission pattern of a dielectric nanoantenna by integrated holographic gratings," *Nano Lett.*, vol. 18, no. 11, pp. 6750–6755, 2018.

[30] P. B. Johnson and R. W. Christy, "Optical constants of the noble metals," *Phys. Rev. B*, vol. 6, no. 12, pp. 4370–4379, 1972.

[31] M. R. Shcherbakov *et al.*, "Ultrafast all-optical switching with magnetic resonances in nonlinear dielectric nanostructures," *Nano Lett.*, vol. 15, no. 10, pp. 6985–6990, 2015.

[32] K. Narayanan and S. F. Preble, "Optical nonlinearities in hydrogenated-amorphous silicon waveguides," *Opt. Exp.*, vol. 18, no. 9, pp. 8998–9005, 2010.

[33] R. Camacho *et al.*, "Nonlinear generation of vector beams from AlGaAs nanoantennas," *Nano Lett.*, vol. 16, no. 11, pp. 7191–7197, 2016.

[34] L. Wang *et al.*, "Shaping the third-harmonic radiation from silicon nanodimers," *Nanoscale*, vol. 9, no. 6, pp. 2201–2206, 2017.

[35] A. B. Evlyukhin, T. Fischer, C. Reinhardt, and B. N. Chichkov, "Optical theorem and multipole scattering of light by arbitrarily shaped nanoparticles," *Phys. Rev. B*, vol. 94, no. 20, 2016, Art. no. 205434.

[36] N. Liu, M. Mesch, T. Weiss, M. Hentschel, and H. Giessen, "Infrared perfect absorber and its application as plasmonic sensor," *Nano Lett.*, vol. 10, no. 7, pp. 2342–2348, 2010.

[37] J. Yao, Y. Yin, L. Ye, G. Cai, and Q. H. Liu, "Enhancing third-harmonic generation by mirror-induced electric quadrupole resonance in a metal-dielectric nanostructure," *Opt. Lett.*, vol. 45, no. 20, pp. 5864–5867, 2020.

[38] J. Yao, H. Hong, N. Liu, G. Cai, and Q. H. Liu, "Efficient third harmonic generation by doubly enhanced electric dipole resonance in metal-based silicon nanodisks," *J. Lightw. Technol.*, vol. 38, no. 22, pp. 6312–6320, Nov. 2020.

[39] P. Grahn, A. Shevchenko, and M. Kaivola, "Electromagnetic multipole theory for optical nanomaterials," *New J. Phys.*, vol. 14, no. 14, pp. 658–666, 2012.